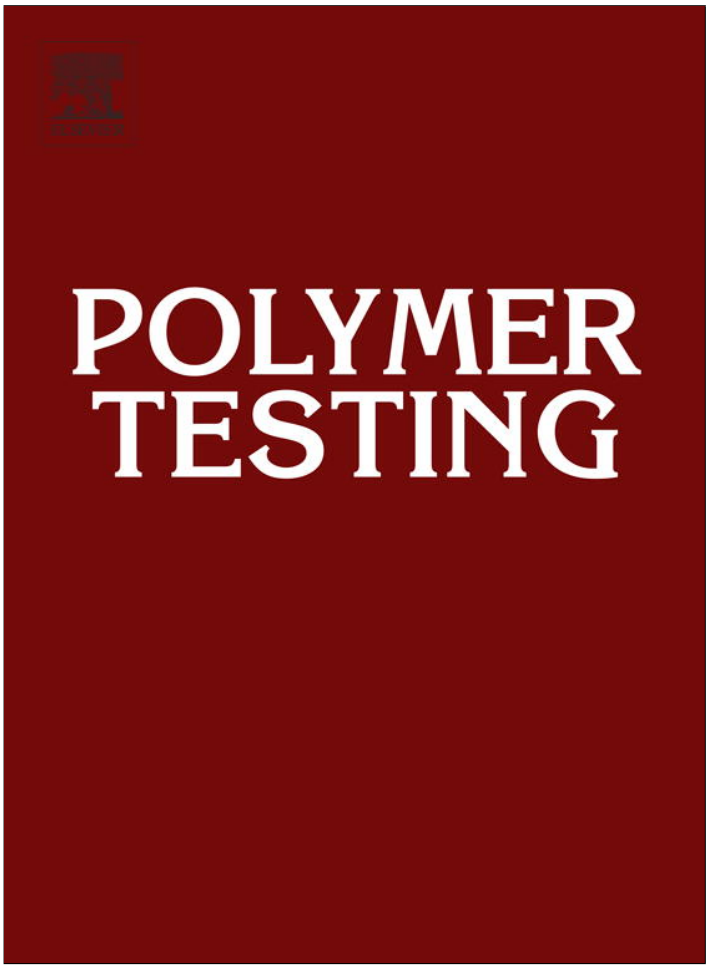

Polymer Testing 32 (2013) 889–900

Contents lists available at SciVerse ScienceDirect

Polymer Testing

journal homepage: www.elsevier.com/locate/polytest

Material properties

Tensile, fracture and impact behavior of transparent Interpenetrating Polymer Networks with polyurethane-poly(methyl methacrylate)

K.C. Jajam [a], S.A. Bird [b], M.L. Auad [b], H.V. Tippur [a,*]

[a] Department of Mechanical Engineering, Auburn University, Auburn, AL 36849, USA
[b] Department of Polymer and Fiber Engineering, Auburn University, Auburn, AL 36849, USA

ARTICLE INFO

Article history:
Received 12 March 2013
Accepted 22 April 2013

Keywords:
Interpenetrating Polymer Networks
Transparent materials
Fracture toughness
Dynamic fracture
Impact behavior
Digital image correlation

ABSTRACT

Transparent Interpenetrating Polymer Networks (IPNs) with poly(methyl methacrylate) (PMMA) as the stiff phase and polyurethane (PU) as the ductile phase with varying PMMA:PU ratios in the range of 90:10 to 70:30 were formulated. Static tensile and fracture tests indicate significant failure strain and crack initiation toughness enhancements with a loss of stiffness relative to PMMA. Dynamic fracture tests were conducted using a long-bar impact loading apparatus in conjunction with an optical method and high-speed photography. Low-velocity impact tests were also performed using a drop-tower. Dynamic fracture and low-velocity impact responses show that an optimum range of PMMA:PU ratios in the IPNs can produce enhanced fracture toughness and impact energy absorption capability when compared to PMMA. Fractographic examination supports macro-measurements by showing a distinct change in surface morphology associated with improved macroscale fracture toughness.

1. Introduction

Lightweight impact-resistant transparent materials are desirable in a wide variety of civilian and military applications, such as hurricane resistant windows, protective eyewear, face shields, helmet visors, aircraft canopies, laser shields and automotive windows. Traditionally, glass has been a transparent structural material in many general and engineering applications [1,2]. Besides its high density, relatively poor fracture resistance and low impact energy absorption characteristics further restrict its use. Interpenetrating Polymer Networks (IPNs) are a relatively new class of materials suitable for the aforementioned applications. IPNs are multiphase polymers comprised of two or more networks which are at least partially interlaced on a molecular scale, but are not covalently bonded to each other and cannot be separated unless individual crosslinks are broken [3]. An example of an IPN is one that combines a thermoplastic polymer with a thermoset where each phase contributes its inherent characteristics to the composite. Thermoplastics offer good ductility but have lower elastic modulus and glass transition temperature (T_g), while thermosets are generally more brittle but stiffer, stronger and have higher T_g. The concept behind IPNs is to combine best features of both types of polymer in order to engineer a new material with optimum stiffness, strength and toughness, while preserving the much needed optical transparency intact. Using this approach, the authors [4] have recently synthesized transparent IPNs with poly(-methyl methacrylate) (PMMA) and polyurethane (PU) as constituents.

Although the term IPN was first coined by Millar [5] in 1960, Aylsworth and Edison were probably the first to

* Corresponding author. Tel.: +1 334 844 3327; fax: +1 334 844 3307.
E-mail addresses: jajamkc@auburn.edu (K.C. Jajam), tippuhv@auburn.edu (H.V. Tippur).

0142-9418/$ – see front matter © 2013 Elsevier Ltd. All rights reserved.
http://dx.doi.org/10.1016/j.polymertesting.2013.04.010

synthesize such a material in 1914 by mixing a crosslinked phenol formaldehyde resin with rubber and sulphur [6,7]. Following these historic works, a great deal of research has been documented on IPNs in the last few decades with emphasis on synthesis, chemistry and morphological aspects [7–9], and thermo-mechanical characterization [10–14].

Despite numerous studies, much of the published research to date on IPNs have resulted in opaque or translucent networks, and very limited work exists from the perspective of transparent IPNs, and relatively few works describe their mechanical performance. Further, they do not provide an insight into their dynamic properties, fracture mechanics at high-rates of loading, or impact energy absorption behavior. These gaps need to be bridged if IPNs are to find applications as windshields and windows in aircrafts, automobile, high-speed trains, armored vehicles and explosive ordinance disposal gear where stress-wave loading dominates. Thus, the primary objective of this study is to investigate mechanical behavior, including fracture response under quasi-static and dynamic loading conditions, and impact energy absorption capability of transparent PMMA-PU IPNs recently synthesized by the authors [4].

2. Materials processing and characterization

2.1. Material preparation

The reagents used for the PMMA system were: methyl methacrylate (MMA, 99%, ACROS Organics), trimethylolpropane trimethacrylate (TRIM, Sigma-Aldrich) and 2,2′-Azobisisobutyronitrile (AIBN, 98%, Sigma-Aldrich), and the reagents for PU system were: poly(tetramethylene ether) glycol (PTMG), 2-Ethyl-2-(hydroxymethyl)-1,3-propanediol (TRIOL, 98%, ACROS Organics), 1,6 diisocyanatohexane (DCH, 99+%, ACROS Organics) and dibutyltin dilaurate (DBTDL, 98%, Pfaltz and Bauer, Inc.). The five different compositions (PMMA:PU ratio) of IPNs were prepared, namely 90:10, 85:15, 80:20, 75:25 and 70:30. A homogeneous mixture was prepared by dissolving the stoichiometric amounts of PTMG, TRIOL and DCH in the MMA monomer and crosslinking agent TRIM. Next, the free-radical initiator, AIBN was dissolved and, finally, the calculated amount of DBTDL catalyst was added. After thorough mixing, the mixture was poured into a closed mold which was kept in an oven at 60 °C for 24 h followed by further curing at 80 °C for another 24 h. After curing, the mold was left in the oven at room temperature for another 12 h for cooling. The inset in Fig. 1 shows the photograph of a transparent 80:20 IPN sheet. Additional details regarding IPN synthesis, network morphology, transparency measurement, thermo-mechanical characterization are available in Ref. [4].

2.2. Elastic characterization

The elastic and physical characteristics of IPNs were determined by indirect means using ultrasonic pulse-echo measurement (see [15] for details) at several discrete locations on the cured sheets. The longitudinal (C_L) and shear (C_S) wave speeds were determined by measuring transit time for the elastic pulse to travel twice the thickness of the sample and, subsequently, the dynamic elastic modulus (E_d) and Poisson's ratio (ν_d) were evaluated. The values of Poisson's ratio in these IPNs were found to be nearly constant at 0.351 ± 0.018. The measured values of C_L, C_S and E_d are shown in Fig. 1. The effect of compositional differences on measured properties is quite evident. The wave speeds and the dynamic elastic modulus show a monotonic decrease as the PU content increases.

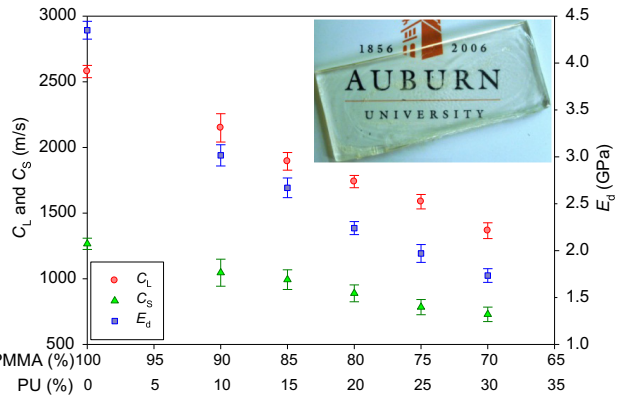

Fig. 1. Measured dynamic material properties of PMMA and IPNs using ultrasonic pulse-echo method. The inset shows a PMMA:PU (80:20) IPN sheet (Dimensions: 170 mm × 80 mm × 8 mm).

2.3. Specimen fabrication and geometry

The cured IPN sheets of 4 mm thickness were machined to dumbbell shaped specimens for tension tests as per ASTM D638 standard [16]. For quasi-static fracture tests, the IPN sheets were machined into rectangular beams of nominal dimensions 100 mm × 20 mm × 8–9 mm (span 80 mm). For dynamic fracture experiments, plate specimens of dimensions 60 mm × 30 mm × 4.5 mm were fabricated. A 6 mm edge notch was cut into both types of specimens using a diamond impregnated wafer blade. The notch tip was sharpened using a razor blade [17]. The dynamic fracture experiments were performed using 2D digital image correlation (DIC) technique to quantify crack tip deformations and fracture parameters. Hence, a random speckle pattern was created on the specimen surface by spraying a fine mist of black and white paints successively. The low-velocity impact tests specimens were fabricated as circular discs of diameter 110 mm and thickness 6 mm.

3. Experimental details

3.1. Tensile testing

The uniaxial tension tests were carried out in an Instron model 4465 testing machine under displacement controlled conditions (crosshead speed = 2 mm/min). Typically, four specimens were tested for each IPN category.

3.2. Quasi-static fracture tests

The quasi-static tests were performed in accordance with ASTM D5045 guidelines [18]. The single edge notched

bend (SENB) specimens were loaded in displacement control mode (cross-head speed = 0.25 mm/min) using an Instron 4465 testing machine. The load-deflection data was recorded up to crack initiation and during stable crack growth, if any, and the mode-I crack initiation toughness, K_{Ic}, was calculated using the peak load. Again, at least four sets of tests were performed for each category. The K_{Ic} for a SENB specimen was calculated using Eq. (1),

$$K_{Ic} = \frac{3\frac{PS}{BW^2}\sqrt{a}}{2\left(1+2\frac{a}{W}\right)\left(1-\frac{a}{W}\right)^{3/2}} \times \left[1.99-\frac{a}{W}\left(1-\frac{a}{W}\right)\left\{2.15-3.93\left(\frac{a}{W}\right)+2.7\left(\frac{a}{W}\right)^2\right\}\right] \quad (1)$$

where P, S, B, W and a are the load at fracture, the span, the thickness, the width and the crack length of the specimen, respectively.

3.3. Dynamic fracture tests

3.3.1. Experimental setup and testing procedure

The 2D DIC method coupled with high-speed photography was used to study dynamic fracture behavior of IPNs. The details regarding the DIC approach and image analysis can be found in Refs. [19,20]. Fig. 2(a) shows the photograph of a specimen and impact loading configuration for dynamic fracture tests. The dotted box represents a 28 × 28 mm^2 region-of-interest. Soft blocks of putty were used to ensure symmetry of the reflected stress-waves from the top and bottom edges of the specimen, and hence loading the crack symmetrically to achieve mode-I fracture conditions. A schematic representation of the experimental setup used in this study is shown in Fig. 2(b). It consisted of a long-bar impactor [21] to deliver load to the specimen dynamically and a Cordin-550 high-speed camera for recording the fracture event in real-time. The high-speed camera records images on 32 individual 1000 × 1000 pixel CCD sensor array positioned circumferentially around a five-facet rotating mirror which reflects and sweeps light over these sensors (see Ref. [17] for optical details). As shown in Fig. 2(b), the camera was focused on a 28 × 28 mm^2 region-of-interest in the crack tip vicinity. Prior to impacting the specimen, a set of 32 reference (undeformed set) images were recorded at a chosen framing rate. While keeping all camera settings the same, the striker was launched. When the striker impacted the long-bar, it generated a compressive stress wave that propagated the length of the bar before imparting a transient load to the specimen edge. The compressive stress waves then entered the specimen, reflected back as tensile waves loading the crack-tip. When the striker contacted the long-bar, an electrical circuit was closed to activate the camera with a user-specified delay to trigger the two high-energy flash lamps. This delay provided sufficient time for the compressive stress wave to travel the length of the long bar to the specimen crack tip as well as enough time for the flash lamps to ramp up to their full intensity levels to provide uniform illumination. The second set of 32 images (deformed set) was captured during the specimen failure. In order to capture the entire fracture event, a framing rate ranging from 250,000–300,000 frames per second was used. A total of 32 images were present in each undeformed and deformed sets. The corresponding images recorded by each of the sensors were paired and analyzed to get crack-opening and crack-sliding displacement fields.

3.3.2. Evaluation of crack velocity and stress intensity factors

Each speckle image from the deformed set was digitized to locate the current position of the crack tip. Subsequently,

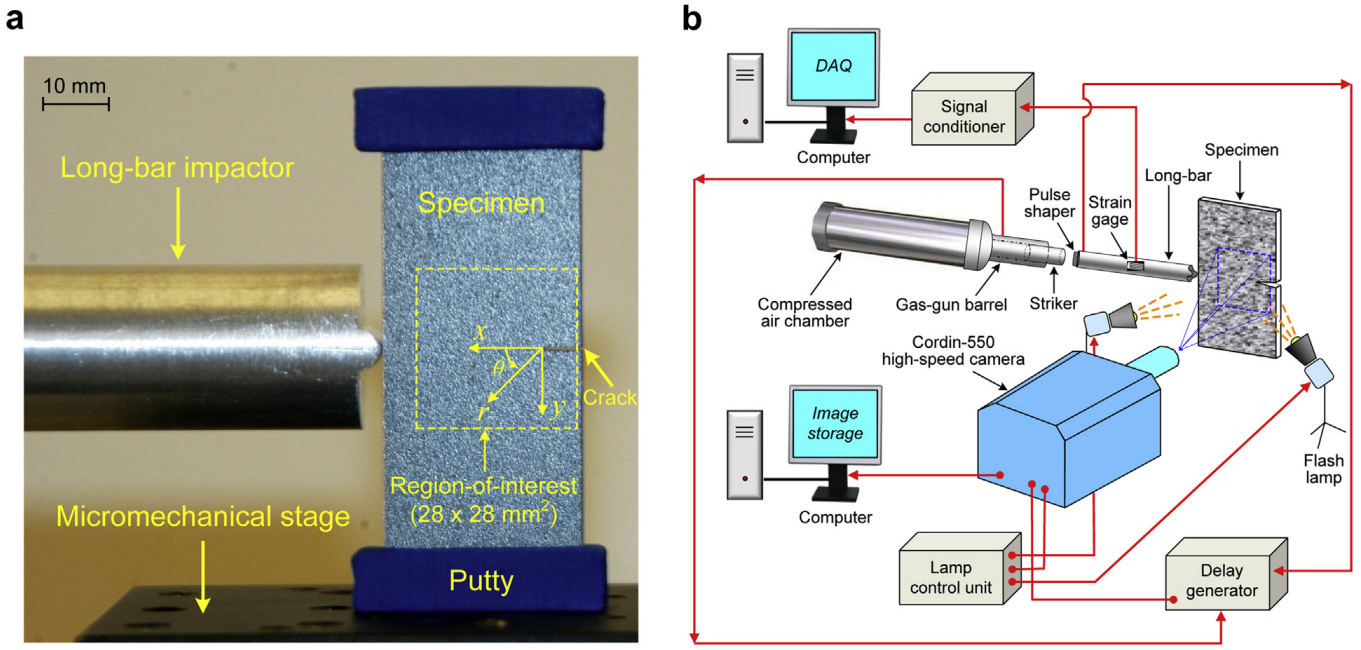

Fig. 2. (a) Close-up view of the long-bar impactor loading and the specimen with random speckle pattern. (b) Schematic of the experimental setup for dynamic fracture study.

the crack velocity (V) was estimated from the crack length history [22]. A sub-image size of 26 × 26 pixels was chosen for correlation to generate 37 × 37 vector grid for both crack-opening (v) and crack-sliding (u) displacement fields. The mode-I stress intensity factors (SIF) were evaluated using an over-deterministic least-squares analysis [23] of displacement fields. The governing asymptotic expression for v and u fields near the tip of a steadily growing crack is given by Eq. (2) [24],

$$\left\{\begin{array}{c} u(r,\theta) \\ v(r,\theta) \end{array}\right\} = \sum_{n=1}^{\infty} \frac{\left(K_{\mathrm{I}}^{\mathrm{d}}\right)_n B_{\mathrm{I}}(V)}{2\mu}\sqrt{\frac{2}{\pi}}(n+1)\left\{\begin{array}{c} r_1^{n/2}\cos\frac{n}{2}\theta_1 - h(n)r_2^{n/2}\cos\frac{n}{2}\theta_2 \\ -\beta_1 r_1^{n/2}\sin\frac{n}{2}\theta_1 + \frac{h(n)}{\beta_2}r_2^{n/2}\sin\frac{n}{2}\theta_2 \end{array}\right\} \tag{2}$$

where

$$\begin{gathered} r_m = \sqrt{x^2+\beta_m^2 y^2}, \quad \theta_m = \tan^{-1}(\beta_m y/x), \quad m = 1,2, \quad \beta_1 = \sqrt{1-(V/C_{\mathrm{L}})^2}, \quad \beta_2 = \sqrt{1-(V/C_{\mathrm{S}})^2} \\ C_{\mathrm{L}} = \sqrt{\frac{(\kappa+1)\mu}{(\kappa-1)\rho}}, \quad C_{\mathrm{S}} = \sqrt{\frac{\mu}{\rho}}, \quad \kappa = (3-\nu_d)/(1+\nu_d) \text{ for plane stress} \\ h(n) = \left\{\begin{array}{l} 2\beta_1\beta_2/\left(1+\beta_2^2\right) : n \text{ odd} \\ \left(1+\beta_2^2\right)/2 : n \text{ even} \end{array}\right., \quad B_{\mathrm{I}}(V) = \frac{\left(1+\beta_2^2\right)}{D}, \quad D = 4\beta_1\beta_2 - \left(1+\beta_2^2\right)^2. \end{gathered} \tag{3}$$

In the above equations, (r, θ) and (x, y) are the instantaneous polar and Cartesian coordinates, respectively, defined at the current crack-tip, C_{L} and C_{S} are longitudinal and shear wave speeds of the material, ρ is the mass density, μ and ν_{d} are the dynamic shear modulus and Poisson's ratio, respectively. The coefficient $(K_{\mathrm{I}}^{\mathrm{d}})_n$ of the dominant terms ($n = 1$) is the so-called mode-I dynamic SIF. In order to extract SIF history, a number of data points were collected in the vicinity of the current crack tip $0.4 < r/B < 1.5$ (where B is the specimen thickness) and ($-150^\circ \le \theta \le -90^\circ$ and $90^\circ \le \theta \le 150^\circ$) to minimize 3D effects on the least-squares method using analytical expressions based on 2D analysis in Eq. (2). Note that Eq. (2) can be reduced to the form of a dynamically loaded stationary crack in the limit the crack velocity $V \to 0$, and was used to extract mode-I SIF history prior to crack initiation.

3.4. Low-velocity impact test setup and testing procedure

For obtaining energy absorption characteristics, low-velocity impact tests were performed according to ASTM D5628 [25] using a drop-tower (Dynatup 9250HV) shown in Fig. 3(a). The instrumented tup (hemispherical head, 12.7 mm diameter) captures the transient contact force response on impact. The specimen support fixture (developed in-house, see Fig. 3(b)) facilitates circular clamp conditions with an aperture of 76.2 mm in diameter. The tests were conducted at a fixed energy level (E) of 60 J with a constant drop-mass (m) 4.85 kg, drop-height (h) 1.27 m, and impact velocity (v_{impact}) 5 m/s. During tests, the specimen was securely clamped into the support fixture. Following drop-height calibration, the cross-head assembly was raised to the desired height and released to impact the specimen. The transient impact load and energy absorbed by the specimen during the entire event was recorded. Note that the Impulse data acquisition software with which the drop-tower is equipped performs energy calculations using the relationship,

$$TE(t) = KE(t) + PE(t) + Ea(t) = \text{constant} \tag{4}$$

where $TE(t)$ is the total energy in the system, which remains constant by the conservation principle, $KE(t)$ is the kinetic energy of the drop-weight, $PE(t)$ is the potential energy of the drop-weight, and $Ea(t)$ is the impact energy absorbed by the specimen up to time t. Graphically, $Ea(t)$ is simply the area under the load-deflection curve and calculated using the mass (m), velocity ($v(t)$), and position ($x(t)$) of the drop-weight,

$$Ea(t) = \frac{1}{2}m\left[v_{impact}^2 - v^2(t)\right] + mgx(t) \tag{5}$$

where the quantities $v(t)$ and $x(t)$ are evaluated using trapezoidal approximations.

4. Results and discussion

4.1. Tensile behavior

The tensile responses of transparent IPNs are shown in Fig. 4. The insets depict the variation of elastic modulus as a function of IPN composition, and a photograph of a failed dumbbell specimen. From the representative stress-strain curves, it can be seen that the initial response in each case indicates a linear elastic region, with a modest nonlinearity before failure in the case of neat PMMA, compared to the IPNs which show a substantial nonlinear response. The IPNs 90:10, 85:15 and 80:20 show yielding at ~50, ~28 and ~25 MPa,

Fig. 3. Experimental setup for low-velocity impact tests: (a) Instron Dynatup 9250HV drop-tower. (b) Close-up view of the impactor tup and the specimen support fixture.

respectively, followed by some strain hardening before failure. In 75:25 and 70:30 IPNs, a yield plateau can be seen between ~4 and ~20% strain followed by appreciable strain hardening until failure. Note that, while the ultimate stresses decrease, a substantial increase in failure strains with increasing PU content occur. The elastic modulus for each specimen was determined by constructing a tangent to the initial part of the stress-strain curve. Each data point represents an average of four measured values of Young's modulus, and the error bars correspond to their standard deviation. It can be seen that there is a monotonic reduction in elastic modulus as the PU phase increases. The trends of gradual drop in tensile strength and Young's modulus with a substantial gain in failure strain with PU content are similar to those reported in [10,14]. Furthermore, this behavior is possibly due to the alteration of chain density as a result of stretching of polymer chains by the interpenetration of one network into the other [26].

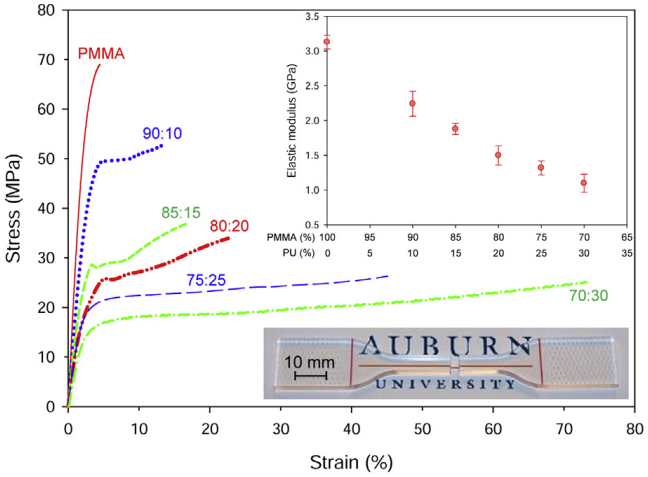

Fig. 4. Typical stress-strain response from tension tests. (The insets show the variation of elastic modulus as a function of IPN composition and a photograph of a failed dumbbell specimen.)

4.2. Quasi-static fracture response

The quasi-static fracture response of IPNs relative to neat PMMA is shown in Fig. 5. The normalized load-deflection curves for all compositions are shown in Fig. 5(a). It can be seen that the curves are generally linear in the initial stage of deformation for each composition. The PMMA shows a linear response up to a peak load followed by a sudden drop, signaling crack initiation. However, in case of IPNs, as the applied load increases, the specimens respond with a modest nonlinearity before reaching the peak load, and again the extent of nonlinearity increases with PU content. This nonlinearity in the pre-peak load region is attributed to crack-tip blunting and crazing prior to crack initiation. Moreover, propagation of the macro-crack is dependent on the increase in the applied load. Further, the crack may deviate from its original propagation plane. It can also be

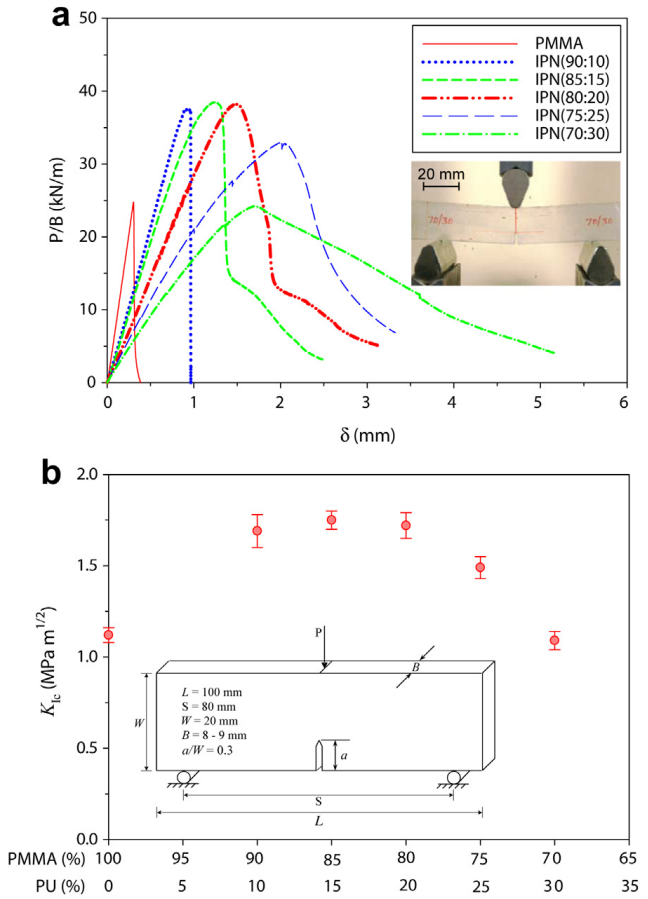

Fig. 5. Quasi-static fracture response: (a) Normalized load-deflection curves. (b) Variation of quasi-static crack initiation toughness (K_{Ic}) as a function of IPN composition.

noted that PMMA and 90:10 IPN indicate brittle unstable crack growth, whereas 85:15 and 80:20 IPNs reveal both brittle as well as stable crack growth. The extensive crack tip blunting followed by stable crack growth is seen in 75:25 and 70:30 IPNs. Also, note that at peak load for each specimen, the corresponding load point deflections increase as the PU content increases in IPNs. Furthermore, the overall deflection also increases with increasing PU phase, and the area under these curves represents the strain energy absorbed. The quasi-static crack initiation toughness, K_{Ic}, was calculated using the load at crack initiation in each case, and its variation as a function of IPN composition is shown in Fig. 5(b). Each data point is again an average of four measured values of K_{Ic}. Approximately 60% improvement in K_{Ic} is evident for IPNs relative to neat PMMA. The trends in K_{Ic} values with increasing PU suggest that there is an optimum range of PMMA:PU ratio for which the quasi-static fracture toughness is the highest. In this work, the 90:10, 85:15 and 80:20 IPNs showed the highest quasi-static crack initiation toughness.

4.3. Dynamic fracture behavior

4.3.1. Surface deformations

A few representative speckle images of the 28 × 28 mm^2 region-of-interest for PMMA and IPNs where surface deformations were monitored optically during dynamic fracture are shown in Fig. 6. The specimens were subjected to symmetric 1-point impact loading on the edge ahead of the initial notch. The time instant (t) after impact at which the images were recorded is also shown, and the position of the propagating crack-tip is indicated by an arrow. Note that different trigger delays were assigned for each specimen category depending on the time taken by the stress waves to load the crack-tip. This enabled capturing a sufficient number of images before and after crack-initiation within the observation window.

As described earlier, a sub-image size of 26 × 26 pixels was chosen for correlation, and displacement fields were obtained as 37 × 37 array of data points for each pair. Subsequently, full-field in-plane displacement contours with 10 μm per contour interval were generated. A few representative speckle images immediately after crack initiation with corresponding crack-opening (v-field or displacement along the y-axis) and crack-sliding (u-field or displacement along the x-axis) displacement contours for PMMA, 85:15 and 75:25 IPNs are presented in Fig. 7. The crack-tip is located at the tip of the arrow in each speckle image. The v- and u-fields show that contour lines and magnitude of displacement (in μm shown by color-bars) are nearly symmetric relative to the crack, consistent with mode-I fracture behavior. By comparing the color bars of the v-field, it can be seen that the crack-opening displacement range is higher in IPNs than for PMMA, with larger deformations in the 85:15 IPN case. The u-field plot shows a set of isolines emerging from the right-hand side of the contour plots due to impact loading on the edge of the specimen ahead of the initial crack-tip.

4.3.2. Crack velocity histories

The crack-tip velocity (V) histories were estimated from the instantaneous values of crack extension data, and are shown in Fig. 8(a). Here, t_i denotes the time at crack initiation after impact. It can be seen that, following initiation, the crack accelerated to attain a maximum speed, followed by an oscillatory growth behavior. The steady state crack velocities (average values in the time window after rapid acceleration) for PMMA are higher than (~350 m/s) all the other specimens tested. On the contrary, IPN samples with PMMA:PU

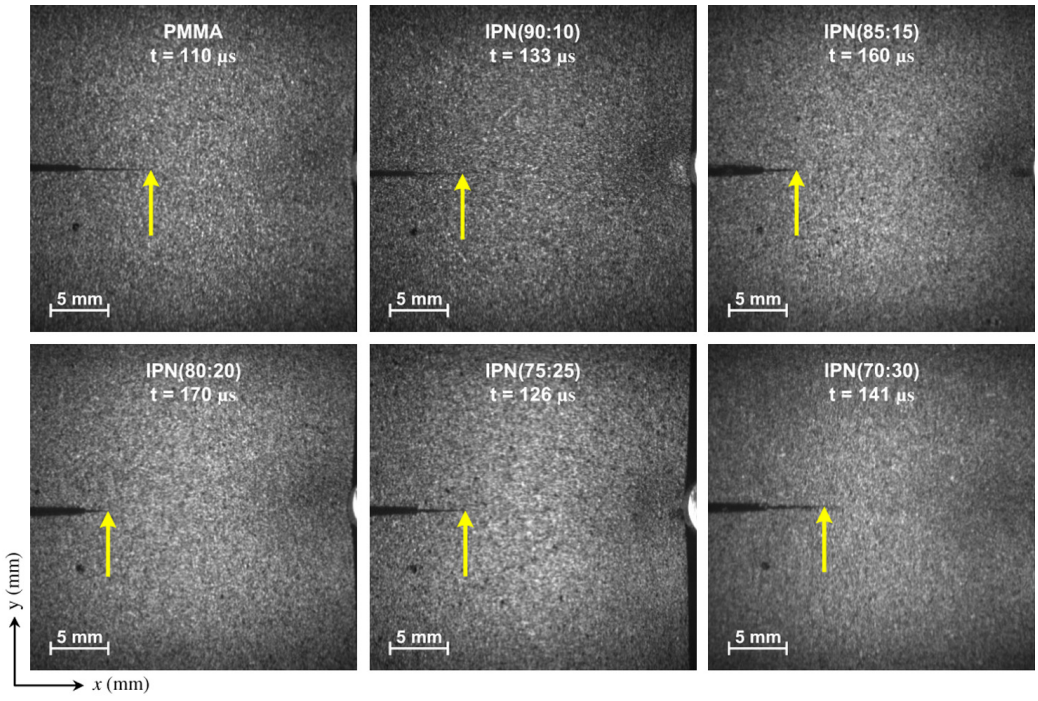

Fig. 6. Selected speckle images of 28 × 28 mm^2 region-of-interest for PMMA and IPNs at different time instants recorded by high-speed camera. The arrow in each image indicates the instantaneous crack-tip position.

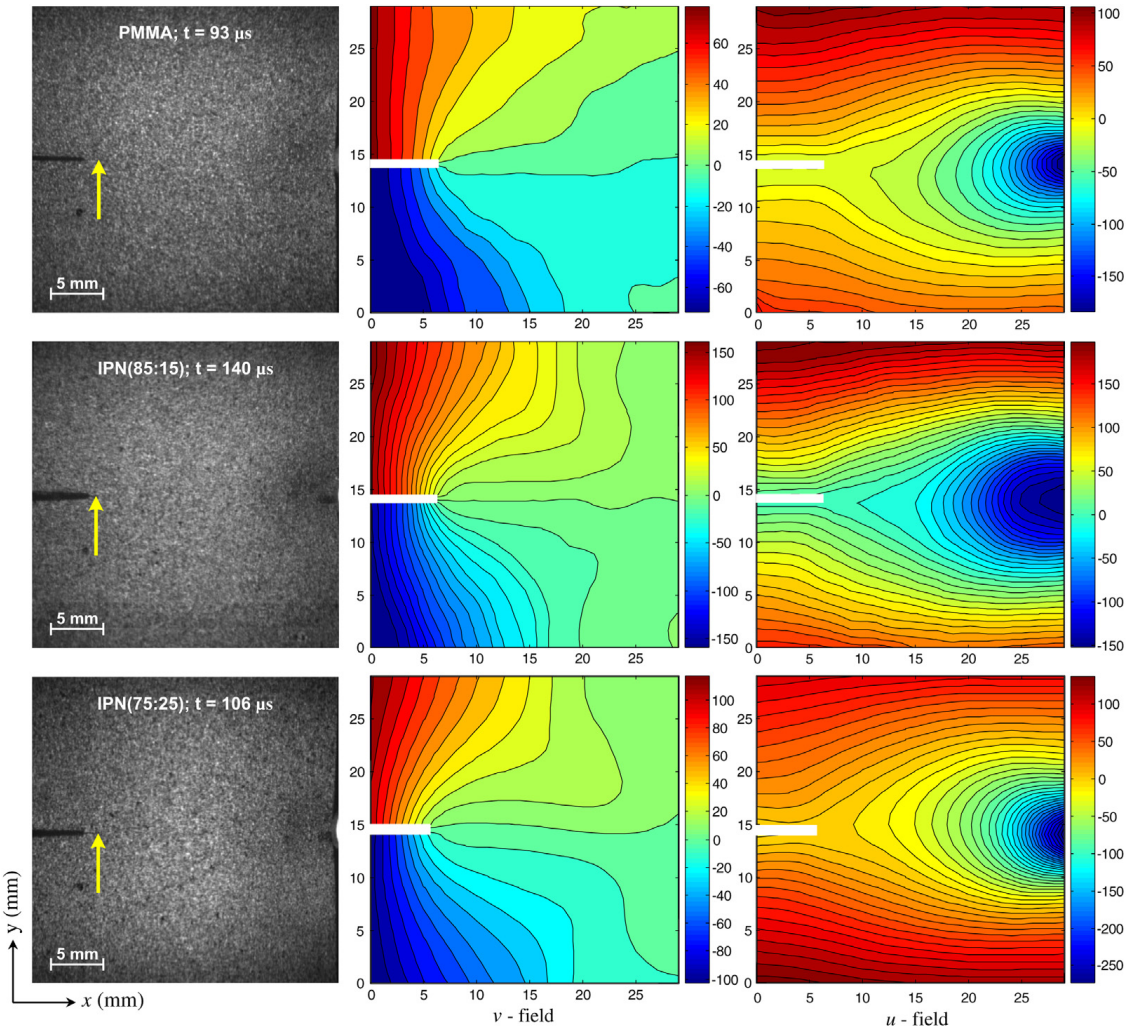

Fig. 7. Measured crack-opening (v-field) and crack-sliding (u-field) displacement contours immediately after crack initiation with corresponding speckle images of 28 × 28 mm^2 region-of-interest. Contour interval is 10 μm. Color-bars represent displacement in μm. The arrows indicate the instantaneous crack-tip position in the speckle images. (For interpretation of the references to color in this figure legend, the reader is referred to the web version of this article.)

ratio of 85:15 and 80:20 show the lowest crack speeds (~100 m/s). Further, for other compositions, the crack speed drops with increasing PU content up to the composition of 80:20, but begins to rise beyond this. That is, 75:25 and 70:30 ratios show higher crack speeds when compared to 80:20 and 85:15 IPNs, suggesting a change in the microstructure, and hence the fracture mechanism. The variation of steady state crack velocity (V_{ss}) as a function of IPN composition is depicted in Fig. 8(b). The 85:15 and 80:20 IPNs show the lowest values of V_{ss}. The variation of V_{ss} also indicates that further increase or decrease in PU content results in an increase in V_{ss}.

4.3.3. Stress intensity factor (SIF) histories

The measured mode-I dynamic SIF histories are presented in Fig. 9(a). In this plot, the crack initiation time is denoted by $t - t_i = 0$. Hence, the negative and positive values correspond to the pre- and post-initiation periods, respectively. In the pre-initiation regime, the dynamic SIF, K_I^d, increases monotonically for each specimen until it reaches a threshold for crack initiation. The K_I^d values in the pre-initiation and post-initiation regimes are higher for 85:15 and 80:20 IPNs when compared to the other cases. The dynamic mode-I crack initiation SIF (K_{Icr}^d) (corresponding to $t - t_i = 0$ as indicated by the vertical dashed line) initially increases with the PU content. That is, relative to PMMA, a modest improvement in 90:10 IPN can be noted. On the other hand, the 85:15 and 80:20 IPNs show approximately 40% enhancement (from ~1.6 MPa m$^{1/2}$ to ~2.25 MPa m$^{1/2}$) in K_I^d at crack initiation. However, when the PU content is increased further, there is a precipitous drop in values for 75:25 and 70:30 compositions. Furthermore, these trends continue into the post-initiation regime ($t - t_i > 0$). Based on these and the previously discussed velocity histories, an optimum IPN composition appears to be in the neighborhood of 85:15 PMMA:PU ratio. The variation of K_{Icr}^d as a function of IPN composition is shown in Fig. 9(b). The 85:15 and 80:20 IPNs show the highest values of K_{Icr}^d among all the cases.

Note that for fracture at elevated loading rates, the crack took longer to initiate in the case of 85:15 and 80:20 IPNs, indicating that the crack initiation can be delayed by incorporating an optimum amount of PU phase. Moreover, the fracture toughness of a material being essentially resistance to crack initiation and propagation, the crack

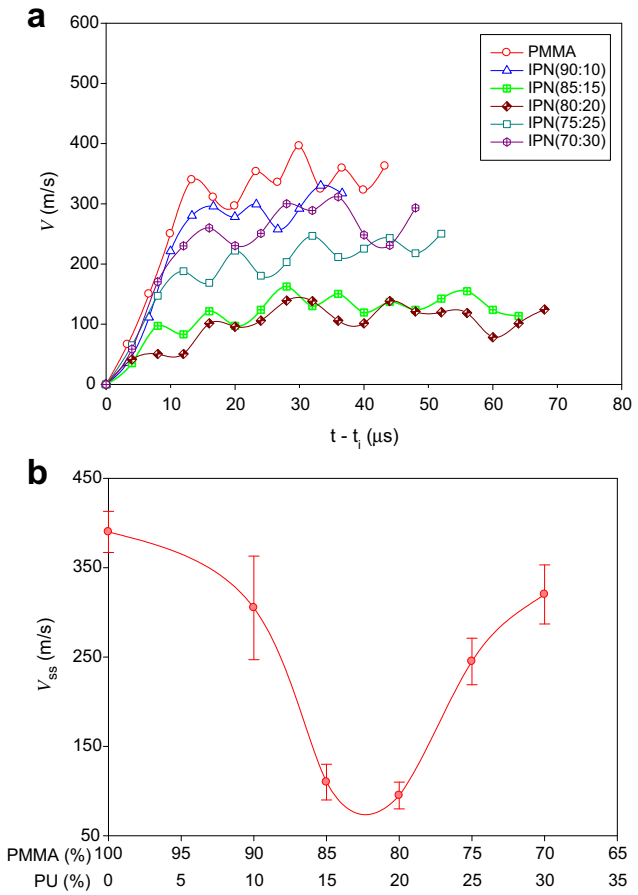

Fig. 8. (a) Measured crack-tip velocity (V) histories for PMMA and various IPNs. (b) Variation of steady state crack velocity (V_{ss}) as a function of IPN composition.

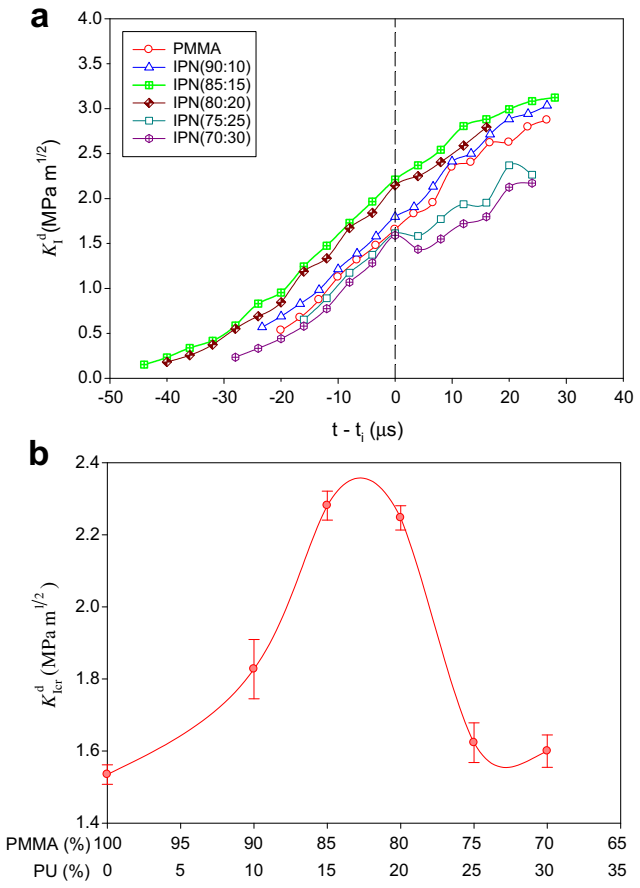

Fig. 9. (a) Measured mode-I dynamic stress intensity factor (K_I^d) histories for PMMA and various IPNs. (Time base is shifted such that $t - t_i = 0$ corresponds to crack initiation as shown by the vertical dashed line.) (b) Variation of mode-I dynamic crack initiation SIF (K_{Icr}^d) as a function of IPN composition.

velocity histories of 85:15 and 80:20 IPNs shows the slowest crack growth (Fig. 8) among all the IPNs.

4.3.4. Fracture surface morphology

Scanning electron microscopy (SEM) was performed on dynamically fractured surfaces. The SEM micrographs of fracture surfaces are shown in Fig. 10. The PMMA fracture surface shown in Fig. 10(a) is nearly featureless with a few conic (parabolic) markings, typical of brittle fracture of neat thermoset polymers and signifying low dissipation of fracture energy. Each parabolic marking is associated with radial lines emanating from its focus. In the case of 90:10 IPN (Fig. 10(b)), the conic marks become smaller in size and increase in number. On the contrary, 85:15 and 80:20 IPN compositions (Figs.10(c) and (d)) (with high dynamic crack initiation toughness) show noticeably textured/rugged surfaces with a high degree of roughness. The creation of new surface is responsible for greater energy dissipation, which explains the higher dynamic crack initiation SIF values seen in these IPNs. However, with further increase of PU content, as in the case of 75:25 (Fig. 10(e)) and 70:30 (Fig. 10(f)) IPNs, a fracture surface resembling that corresponding to the low energy dissipation case returns. In these cases, with higher PU content, the number and density of conic marks increase with a decrease in their size. These transitions in microscopic features are consistent with the drop in crack initiation toughness measured earlier. Note that the conic marks seen in acrylic-based materials under dynamic fracture are consistent and well documented in the literature [27–29]. These studies indicate that at higher crack speeds ($V \geq 0.4\ C_R$, where C_R is the Rayleigh wave speed for PMMA ~850 m/s), the presence of conic markings is a typical feature. In the present work, the average crack speed for PMMA and IPNs showing conic marks are in the range of 300–400 m/s and satisfy the above criterion of ($V \geq 0.4\ C_R$). The conic marks do not appear in 85:15 and 80:20 cases, possibly due to the lower crack speeds (~100 m/s).

4.4. Low-velocity impact response

4.4.1. Energy absorption characteristics

The transient load histories from drop-tower tests are presented in Fig. 11(a), indicating how these materials behave during an impact event. The presence of an initial knee in each case, indicated by the dotted region in the load-time curves, is due to the inertial effects, and can be termed as the inertial loading zone indicating initial contact between the tup and the specimen. During this early stage of impact, the specimen deforms elastically and separates from the tup due to elastic wave reflections. Then the tup re-establishes contact with the specimen and

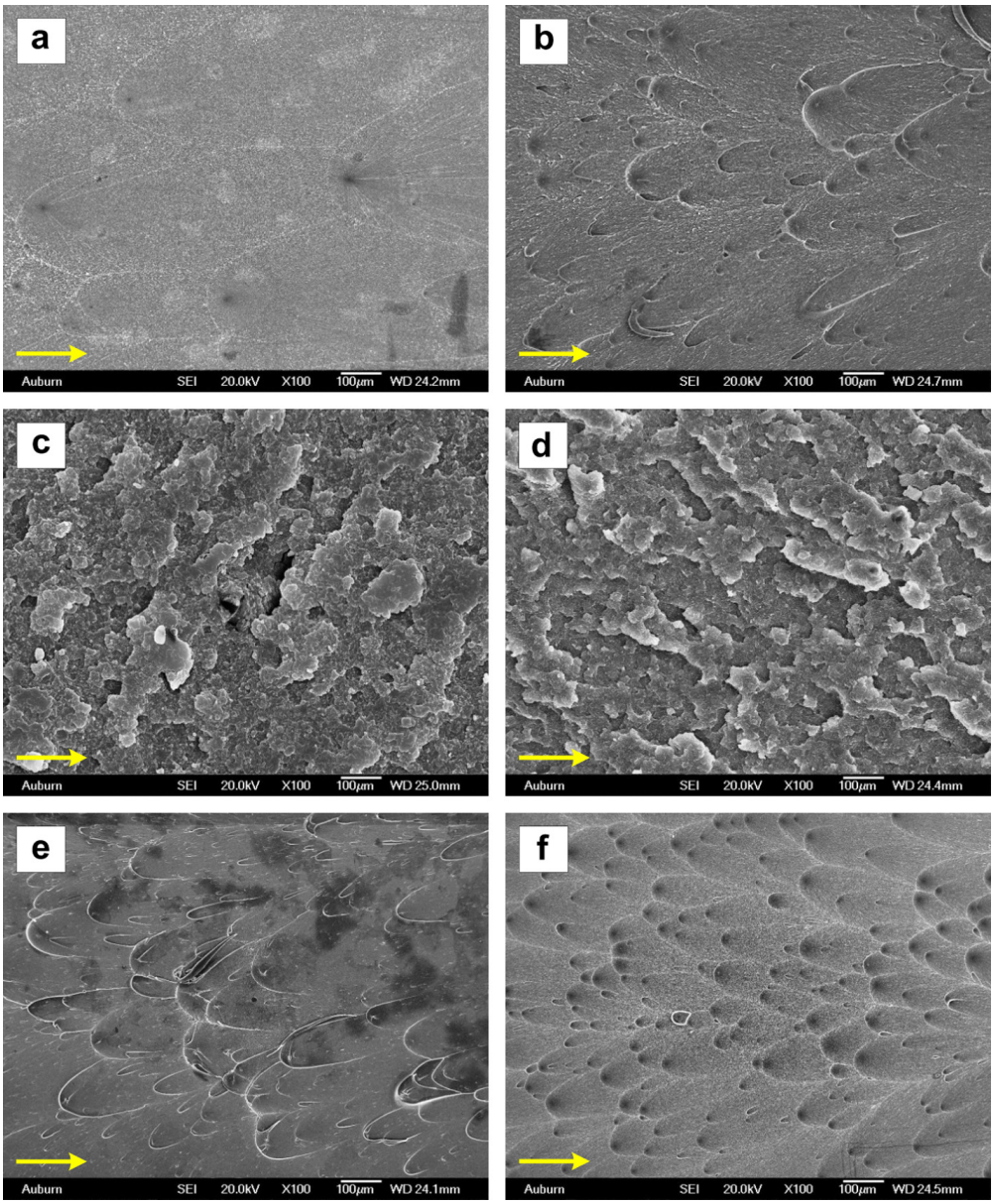

Fig. 10. SEM micrographs of dynamically fractured surfaces: (a) PMMA. (b) 90:10 IPN. (c) 85:15 IPN. (d) 80:20 IPN. (e) 75:25 IPN. (f) 70:30 IPN. The arrow in each micrograph indicates the direction of crack growth.

continues to deform the specimen elastically until it yields. From the transient load history, it can be noted that the slope of the curves relative to PMMA decrease with increasing PU content, with nearly equal slopes for 90:10, 85:15 and 80:20 IPNs. Note that, in a typical transient event such as an impact test, the slope of the load history in the elastic region represents *contact stiffness* [30]. Following elastic deformation and yielding, the load continues to increase until a peak value is attained beyond which a drop in the load signals commencement of damage. After reaching an ultimate load value, the IPNs start to suffer plastic deformation, whereas PMMA shows a steep drop in the load, qualitatively indicating brittle failure. Also note that, of all the cases, 85:15 and 80:20 IPNs sustained maximum peak load before showing a precipitous drop due to failure. Relative to PMMA, the 90:10 IPN shows modest improvement in the load carrying capacity, whereas 75:25 and 70:30 IPNs show lower values of peak load. In terms of failure, the IPNs take longer (5–8 ms) to fail than PMMA (1 ms). The longer duration also indicates progressive damage, whereas shorter time in the case of PMMA signals catastrophic failure.

Fig. 11(b) shows time histories of impact energy absorbed by various IPNs relative to PMMA. A linear region is evident for all specimens followed by deviations from linearity, after which the curves attain a plateau in each case. It should be noted that, in the initial stage of impact loading, the energy absorption in the specimens is mainly through elastic deformation. Beyond this regime, the specimen absorbs energy through plastic deformation and various other damage mechanisms. It can be seen that energy absorption rates decrease with increasing PU content. Also note that the 90:10, 85:15 and 80:20 IPNs again show nearly equal slopes. Further, the duration of energy

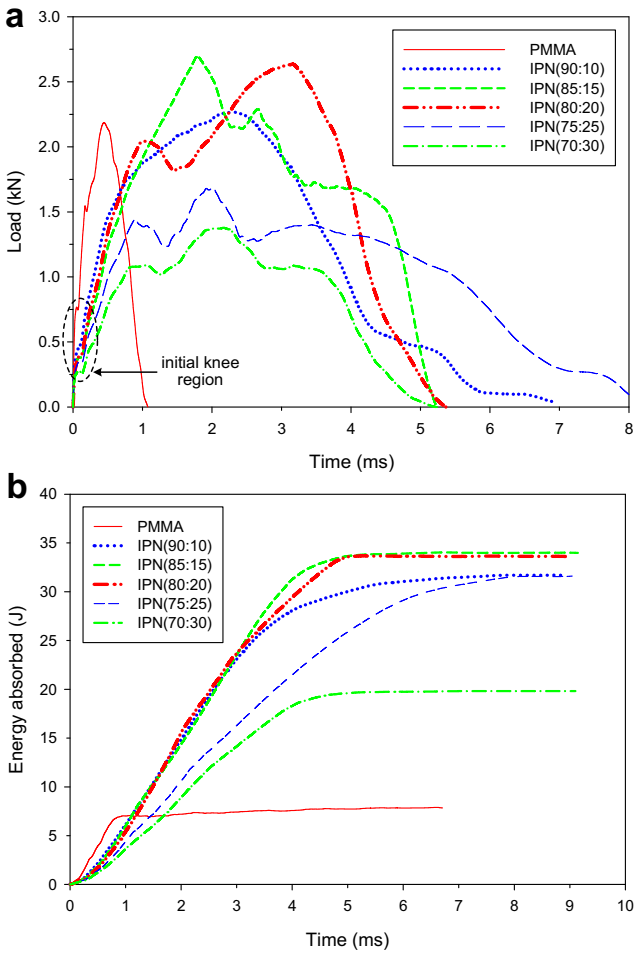

Fig. 11. Low-velocity drop-weight impact tests: (a) Transient load vs. time response. (b) Energy absorbed vs. time response.

absorption for elastic deformation is longer in IPN cases (4–5 ms) than for PMMA (0.75 ms). From Fig. 11(b), it is worth noting that IPNs show tremendous impact energy absorption capabilities when compared to PMMA. Quantitatively, the energy absorbed by IPNs is 3 to 4 times that of PMMA. The energy absorbed is a measure of the toughness of a material which is further defined as an optimum combination of strength and ductility [31]. Also note that, of all IPN compositions, the 85:15 and 80:20 exhibit the highest damage tolerance and energy absorption capabilities under identical impact conditions.

4.4.2. Impact damage features

The photographs depicting macro scale damage features of the front and back surfaces of a few selected specimens are shown in Fig. 12. During impact, the front (or top) surface experiences a compressive transient load causing tensile failure of the back (or bottom) surface. In all the failed specimens, through-the-thickness cracks emanate from the impact point. However, the number of cracks, their length and growth behaviors differ. PMMA, being a brittle material compared to the IPNs, fails catastrophically, evidenced by a circular opening due to the complete penetration of the indenter. The main failure mode in this case is spallation around the circular opening followed by the growth of radial cracks. In the case of 85:15 IPN, the tup created a small rupture and generated four radial cracks from the impact point. These through-the-thickness cracks made four quadrants on both front and back surfaces of the specimen, propagated ~90° apart relative to each other, and terminated by forming a shear-craze at the terminal points. Interestingly, the length of the cracks in 85:15 IPN is the longest of all the cases shown here. The failure pattern of 80:20 IPN (not shown) also involved four radial cracks propagated ~90° apart relative to each other. In this case

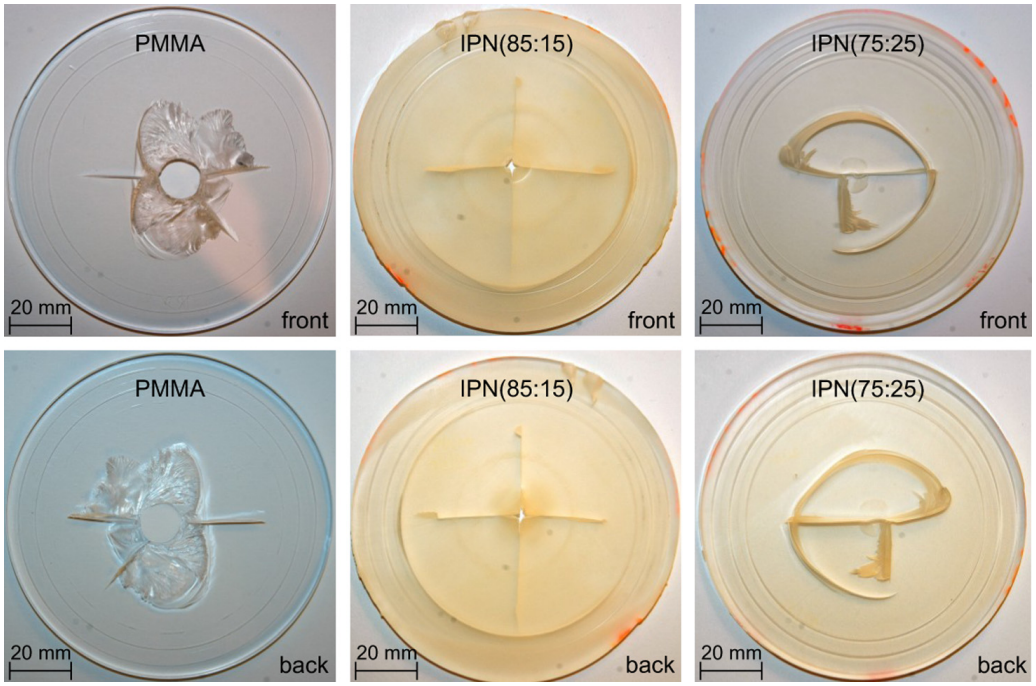

Fig. 12. Selected photographs of front and back surfaces of samples subjected to low-velocity drop-weight impact tests.

also, the cracks terminated at a (nearly) circular crack due to the flexural failure of the petals. In the case of 75:25 and 70:30 (not shown) IPNs, only three radial cracks are visible confined by a tri-quadrant crack joining the failed petals. The crack lengths in 80:20, 75:25 and 70:30 IPN configurations are shorter than the 85:15 IPN. It should be noted that through-the-thickness cracking and shear-crazing are dominant failure modes in the IPNs. Furthermore, there was no material spallation in the IPNs, even after impact damage, and the size of the damage zone got smaller with higher PU content.

5. Conclusions

PMMA-PU based transparent IPNs of different compositions were investigated for static and dynamic properties, including fracture response and impact energy absorption. The DIC method coupled with high-speed photography was used for extracting dynamic fracture parameters. The impact energy absorption characteristics were investigated by performing low-velocity impact tests. The following are some of the major observations of this study:

- Both quasi-static and dynamic elastic moduli gradually decreased as the PU phase increased in IPNs.
- Static tensile tests showed increasing ductility with a loss of strength and stiffness of IPNs as the PU content increased.
- Quasi-static fracture tests indicated brittle unstable crack growth in 90:10 IPN, brittle as well as stable crack growth in the case of 85:15 and 80:20 IPNs, and ductile stable crack growth in 75:25 and 70:30 IPNs. The work up to crack initiation was higher for 85:15 and 80:20 IPNs. The quasi-static fracture toughness was found to be optimum for 90:10, 85:15 and 80:20 IPNs.
- Dynamic fracture tests showed lower crack speeds in IPNs relative to PMMA, with the slowest crack growth in 85:15 and 80:20 IPNs. The dynamic crack initiation toughness enhancement was the highest for 85:15 and 80:20 IPNs.
- The dynamically fractured surfaces of 85:15 and 80:20 IPNs showed highly tortuous fracture surfaces, indicating high energy dissipation during fracture, whereas other cases depicted relatively smooth surfaces.
- All IPNs showed higher impact energy absorption capability relative to PMMA with highest energy absorbed by 85:15 and 80:20 IPNs in low-velocity impact tests.

Acknowledgments

The authors gratefully acknowledge the financial support for this research through a grant HDTRA1-09-1-0023 from the Defense Threat Reduction Agency.

References

[1] A. Macfarlane, G. Martin, Glass: A World History, The University of Chicago Press, Chicago, USA, 2002.
[2] H. Rawson, Properties and Applications of Glass, Elsevier Scientific Publishing Co., 1980.
[3] L.H. Sperling, Interpenetrating Polymer Networks and Related Materials, Plenum Press, New York, USA, 1981.
[4] S.A. Bird, D. Clary, K.C. Jajam, H.V. Tippur, M.L. Auad, Synthesis and characterization of high performance, transparent interpenetrating polymer networks with polyurethane and poly(methyl methacrylate), Polymer Engineering & Science 53 (2013) 716–723.
[5] J.R. Millar, Interpenetrating polymer networks. Styrene-divinylbenzene copolymers with two and three interpenetrating networks, and their sulphonates, Journal of the Chemical Society (1960) 1311–1317.
[6] C. Vasile, A.K. Kulshreshtha, Handbook of Polymer Blends and Composites, vol. 3A, Rapra Technology Ltd., Shawsbury, 2003.
[7] L.H. Sperling, V. Mishra, The current status of interpenetrating polymer networks, Polymers for Advanced Technologies 7 (1996) 197–208.
[8] S.C. Kim, D. Klempner, K.S. Frisch, W. Radigan, H.L. Frisch, Polyurethane interpenetrating polymer networks. I. Synthesis and morphology of polyurethane-poly(methyl methacrylate) interpenetrating polymer networks, Macromolecules 9 (1976) 258–263.
[9] N. Gupta, A.K. Srivastava, Interpenetrating polymer networks: a review on synthesis and properties, Polymer International 35 (1994) 109–118.
[10] M. Akay, S.N. Rollins, Polyurethane-poly(methyl methacrylate) interpenetrating polymer networks, Polymer 34 (1993) 1865–1873.
[11] Y.C. Chou, L.J. Lee, Mechanical properties of polyurethane-unsaturated polyester interpenetrating polymer networks, Polymer Engineering & Science 35 (1995) 976–988.
[12] D. Chakrabarty, B. Das, S. Roy, Epoxy resin–poly(ethyl methacrylate) interpenetrating polymer networks: morphology, mechanical, and thermal properties, Journal of Applied Polymer Science 67 (1998) 1051–1059.
[13] I. Harismendy, M. Del Río, C. Marieta, J. Gavalda, I. Mondragon, Dicyanate ester–polyetherimide semi-interpenetrating polymer networks. II. Effects of morphology on the fracture toughness and mechanical properties, Journal of Applied Polymer Science 80 (2001) 2759–2767.
[14] A. Morin, H. Djomo, G.C. Meyer, Polyurethane-poly(methyl methacrylate) interpenetrating polymer networks: some mechanical properties, Polymer Engineering and Science 23 (1983) 394–398.
[15] P.R. Marur, H.V. Tippur, Evaluation of mechanical properties of functionally graded materials, Journal of Testing and Evaluation 26 (1998) 539–545.
[16] ASTM, D638-01, Standard Test Method for Tensile Properties of Plastics, Annual Book of ASTM Standards, 2001, pp. 45–57.
[17] K.C. Jajam, H.V. Tippur, An experimental investigation of dynamic crack growth past a stiff inclusion, Engineering Fracture Mechanics 78 (2011) 1289–1305.
[18] ASTM, D5045-96, Standard Test Methods for Plane-strain Fracture Toughness and Strain Energy Release Rate of Plastic Materials, Annual Book of ASTM Standards, 1996, pp. 325–333.
[19] M.S. Kirugulige, H.V. Tippur, T.S. Denney, Measurement of transient deformations using digital image correlation method and high-speed photography: application to dynamic fracture, Applied Optics 46 (2007) 5083–5096.
[20] K.C. Jajam, H.V. Tippur, Quasi-static and dynamic fracture behavior of particulate polymer composites: a study of nano- vs. micro-size filler and loading-rate effects, Composites Part B: Engineering 43 (2012) 3467–3481.
[21] R. Bedsole, H.V. Tippur, Dynamic fracture characterization of small specimens: a study of loading rate effects on acrylic and acrylic bone cement, ASME Journal of Engineering Materials and Technology 135 (2013) 031001.
[22] K.C. Jajam, H.V. Tippur, Role of inclusion stiffness and interfacial strength on dynamic matrix crack growth: an experimental study, International Journal of Solids and Structures 49 (2012) 1127–1146.
[23] R. Sanford, Application of the least-squares method to photoelastic analysis, Experimental Mechanics 20 (1980) 192–197.
[24] T. Nishioka, S.N. Atluri, Path-independent integrals, energy release rates, and general solutions of near-tip fields in mixed-mode dynamic fracture mechanics, Engineering Fracture Mechanics 18 (1983) 1–22.
[25] ASTM, D5628-96, Standard Test Method for Impact Resistance of Flat, Rigid Plastic Specimens by Means of A Falling Dart (Tup or Falling Mass), Annual Book of ASTM Standards, 1996, pp. 242–251.
[26] X. Zhao, A theory for large deformation and damage of interpenetrating polymer networks, Journal of the Mechanics and Physics of Solids 60 (2012) 319–332.
[27] J. Fineberg, M. Marder, Instability in dynamic fracture, Physics Reports 313 (1999) 1–108.

[28] J. Scheibert, C. Guerra, F. Célarié, D. Dalmas, D. Bonamy, Brittle-quasibrittle transition in dynamic fracture: an energetic signature, Physical Review Letters 104 (2010) 045501.
[29] C. Guerra, J. Scheibert, D. Bonamy, D. Dalmas, Understanding fast macroscale fracture from microcrack post mortem patterns, Proceedings of the National Academy of Sciences 109 (2012) 390–394.
[30] M.V. Hosur, F. Chowdhury, S. Jeelani, Low-velocity impact response and ultrasonic NDE of woven carbon/epoxy—nanoclay nanocomposites, Journal of Composite Materials 41 (2007) 2195–2212.
[31] R.O. Ritchie, The conflicts between strength and toughness, Nature Materials 10 (2011) 817–822.